A&A, 692, A112 (2024)
https://doi.org/10.1051/0004-6361/202452008

Astronomy & Astrophysics

Unveiling key factors in solar eruptions leading to the solar superstorm in 2024 May

Rui Wang[1,2,3,⋆], Ying D. Liu[1,2,3], Xiaowei Zhao[4,5], and Huidong Hu[1,2]

[1] State Key Laboratory of Space Weather, National Space Science Center, Chinese Academy of Sciences, Beijing 100190, People's Republic of China
[2] Solar Activity and Space Weather, National Space Science Center, Chinese Academy of Sciences, Beijing 100190, People's Republic of China
[3] University of Chinese Academy of Sciences, Beijing, China
[4] Key Laboratory of Space Weather, National Satellite Meteorological Center (National Center for Space Weather), China Meteorological Administration, Beijing 100081, People's Republic of China
[5] School of Earth and Space Sciences, Peking University, Beijing 100871, People's Republic of China

Received 27 August 2024 / Accepted 7 November 2024

ABSTRACT

NOAA active region (AR) 13664/8 produced the most intense geomagnetic effects since the Halloween event of 2003. The resulting extreme solar storm is thought to be the consequence of multiple interacting coronal mass ejections (CMEs). Notably, this AR exhibits exceptionally rapid magnetic flux emergence. The eruptions on which we focus all occurred along collisional polarity inversion lines (PILs) through collisional shearing during a three-day period of extraordinarily high flux emergence ($\sim 10^{21}$ Mx h^{-1}). Our key findings reveal how photospheric magnetic configurations in eruption sources influence solar superstorm formation and geomagnetic responses, and link exceptionally strong flux emergence to sequential homologous eruptions: (1) We identified the source regions of seven halo CMEs that were distributed primarily along two distinct PILs. This distribution suggests two groups of homologous CMEs. (2) The variations in the magnetic flux emergence rates in the source regions are correlated with the CME intensities. This might explain the two contrasting cases of complex ejecta that are observed at Earth. (3) Our calculations of the magnetic field gradients around the CME source regions show strong correlations with eruptions. This provides crucial insights into solar eruption mechanisms and enhances our prediction capabilities for future events.

Key words. Sun: activity – Sun: coronal mass ejections (CMEs) – Sun: magnetic fields – solar-terrestrial relations

1. Introduction

The impact of space weather on human society is increasingly significant. Solar superstorms stand out due to their remarkable geomagnetic effects. Liu et al. (2014, 2019) reported that solar superstorms often form through a mechanism that is known as a "perfect storm", where multiple factors are combined to amplify the intensity of a storm that would otherwise be moderate. These factors typically include the consecutive eruption of multiple coronal mass ejections (CMEs), preconditioning, and CME-CME interactions. Liu et al. (2019) emphasized the particular importance of preconditioning in the generation of Carrington-class solar storms.

These consecutive CMEs often originate from the same active region (AR) or even from the same polarity inversion line (PIL), commonly known as homologous CMEs (Woodgate et al. 1984; Zhang & Wang 2002). They often form in new or highly dynamic ARs exhibiting strong magnetic flux emergence. To initiate a solar eruption, two essential factors are typically required: a magnetic flux-rope (MFR) structure in the eruption source region, and the triggering of this MFR by instability. MFRs can form through two primary mechanisms. Strong photospheric shearing motions can create a twisted MFR through the tether-cutting process (van Ballegooijen & Martens 1989; Moore et al. 2001). In this process, magnetic reconnection occurs and causes a significant amount of magnetic flux to be cancelled and submerged below the photosphere. The coronal magnetic field around the PIL then becomes more strongly sheared and twisted. On the other hand, evidence suggests that twisted magnetic structures already exist beneath the photosphere, and during the process of flux emergence, these twisted structures directly rise to the photosphere as MFRs (Okamoto et al. 2008). When the MFR has formed, instability becomes the key factor that leads to the eventual eruption. It can arise from the MFR itself, such as when a twisted MFR exceeds a critical twist value. This triggers the kink instability (Fan & Gibson 2004; Kliem et al. 2004; Török et al. 2004). It also arises from the confining magnetic fields around the MFR, such as torus instability. This occurs when the Sun-directed Lorentz force decreases faster with height than the radial outward-directed hoop force (Kliem & Török 2006).

Chintzoglou et al. (2019) proposed a scenario called "collisional shearing". This scenario suggests that together with the dynamic flux emergence, collisional shearing processes occur between nonconjugated magnetic polarities. Nonconjugated polarities refer to the interactions between two nondipolar magnetic polarity pairs with opposite polarities. According to Chintzoglou et al. (2019), they indicate that most of the consecutive eruptions occur at these collisional PILs rather than at the PILs of dipolar pairs. Their approach allows for a more accurate measurement of the cancelled magnetic flux during flux emer-

⋆ Corresponding author; rwang@swl.ac.cn

gence. Wang et al. (2022) applied this method to measure the cancelled magnetic flux in AR 11283 and estimated that the cancelled flux accounted for over 24% of the total unsigned flux. This subtantial cancelled flux explains why this AR was able to produce four consecutive major eruptions within the short span of three days. Dhakal & Zhang (2023) used the method proposed by Schrijver (2007) to extract a strong-gradient PIL (SgPIL) and found a strong correlation between SgPIL and flare productivity for superactive ARs. The formation of the SgPIL is strongly associated with the collisional shearing scenario.

The series of eruption events that occurred in 2024 May resulted in a strong geomagnetic response close to that of the Halloween event in 2003, for which the Dst index reached ∼−412 nT. These eruptive events are associated with AR 13664/8, which exhibited exceptionally strong magnetic flux emergence and produced multiple flares of M class and higher, each accompanied by halo CMEs. The intense flux emergence led to an unusually complex magnetic field configuration in the region. In this paper, we mainly focus on how photospheric magnetic configurations in eruption sources influence solar superstorm formation and geomagnetic responses, and link exceptionally strong flux emergence to sequential homologous eruptions. In Sect. 2 we present the data analysis of the magnetic field and imaging results, and in Sect. 3 we draw conclusions and engage in discussions.

2. Data analysis and results

Solar storms have caused prolonged geomagnetic disturbances in which the Dst index rapidly decreased to ∼−412 nT on 2024 May 10 and failed to fully recover to normal levels even after May 13. In their recent study, Liu et al. (2024) analyzed the data and identified a series of consecutive halo CMEs, some of which exhibited a strong southward component. The authors categorized these halo CMEs into two contrasting cases of complex ejecta. It was determined that the four consecutive halo CMEs from May 8 to 9 were the primary contributors to the rapid Dst decline on May 10 (see GOES soft X-ray curve in Fig. 1). Subsequently, three halo eruptions between May 9 17:44 UT and May 11 were identified as the main factors for the sustained and incomplete recovery of the Dst. Readers are directed to Liu et al. (2024) for the indentification and discussion of full-halo CMEs. The characteristics of the source region for these eruptions are yet to be determined.

We determined thorugh examination that the first four eruptions originated from the lower region indicated in Fig. 1, with the axial magnetic field of the MFR aligned roughly along the red arrow and the azimuthal magnetic field along the blue arrows. The southward field distribution explains why these initial four eruptions led to a rapid decrease in the Dst index. The subsequent three eruptions originated from the upper region, with the axial field aligned in the direction of the purple arrow, and the azimuthal field also underwent a significant reversal and approached a northward orientation of the magnetic field. The subsequent eruptions that continued to include X-class eruptions after May 11 are not further discussed because they were very close to the limb or on the far side of the Sun.

This AR was formed by the convergence of two neighboring ARs (AR 13664/8) through a process that is known as collisional shearing. The complex AR underwent a fast flux emergence, with a continuous increase in unsigned flux, and it exhibited an extraordinary magnetic flux emergence rate (see Fig. 2a). We calculated the unsigned magnetic flux for May 5-11 from the Solar Dynamics Observatory's (SDO; Pesnell et al. 2012) Helioseismic and Magnetic Imager (HMI; Scherrer et al. 2012; Schou et al. 2012) data series hmi.sharp_cea_720s_dconS, which offers improved quality for the flux calculations. Our analysis focused on pixels with field strengths exceeding 200 G. The unsigned flux reached a maximum of $\sim 1.5 \times 10^{23}$ Mx by the end of May 11. Most remarkably, the 6-hour average flux emergence rate peaked at an exceptional $\sim 1.6 \times 10^{21}$ Mx h^{-1} on May 8. This rate is truly extraordinary and surpasses even the most notable ARs of recent solar cycles, including AR 12673, which caused the most intense flare of cycle 24, and AR 12192, which was the largest sunspot group observed since 1990. In the Stanford HMI science nuggets, Sun et al. (2024)[1] indicated that this event likely representsed the most rapid flux emergence ever recorded in the SDO era. It marks a historic milestone in solar observations. Our findings, while showing a slightly lower peak of the unsigned magnetic flux, strongly support this assertion. The emergence rate profile reveals a primary peak on May 8 that was flanked by substantial secondary peaks on May 7 and 9 (Fig. 2a). Notably, the average emergence rate over this three-day period sustained an extraordinarily high magnitude of $\sim 10^{21}$ Mx h^{-1}.

When the magnetic field threshold is adjusted to 150 G, our results align closely with those reported by Sun et al. (2024). This further confirms the historical significance of this event. This extraordinary flux emergence rate not only sets a new benchmark for solar activity observations, but also challenges our understanding of the underlying mechanisms that drive these extreme events.

We focus on five eruptions (E1-E5) from May 8 to 9 within a longitude of ±30°, where the magnetic field data are considered to be more reliable (Hoeksema et al. 2014), and we provide source imaging for two additional eruptions (E6 and E7) outside this range as reference. They correspond to CMEs 1-7 in Liu et al. (2024). In the extreme-ultraviolet (EUV) imaging data captured by the Atmospheric Imaging Assembly (AIA; Lemen et al. 2012) on board SDO, we observe a filament or hot channel structures in the eruption source region (Fig. 2b-2h). Except for E1, where the filament is visible in the relatively cooler 304 Å wavelength channel (along the north-south direction), the remaining eruptions can only be observed in the hotter 131 Å, indicating that the continuous eruptions have heated the source region significantly. By analyzing the onset of the EUV brightening, we can roughly determine the location of the PILs corresponding to the eruption source region. E5 exhibits a large-scale hot channel structure, but the primary eruption source region is likely associated with the brightening structure above the strong magnetic field region.

Figure 3 presents the magnetograms and magnetic field gradient distribution corresponding to the eruptions. We used the line-of-sight (LOS) magnetic field data instead of Spaceweather HMI Active Region Patches (SHARPs; Bobra et al. 2014; Hoeksema et al. 2014) for two reasons: First, scientific SHARP data are currently unavailable, and second, the SHARP data for May 8 miss several hours of observations. The LOS magnetic field data provide a continuous and reliable alternative for our analysis. We followed the method used for processing SHARP data to handle the LOS magnetic field data. Initially, we preprocessed full-disk 45 s LOS magnetograms at a time interval of 720 s to account for the satellite rotation that occurred between 16:00 and 24:00 UT on May 8. Subsequently, we created cutout maps from these full-disk LOS observations, with a field of view of 1000×600 pixels, which is large enough to encompass the AR,

[1] http://hmi.stanford.edu/hminuggets/?p=4216

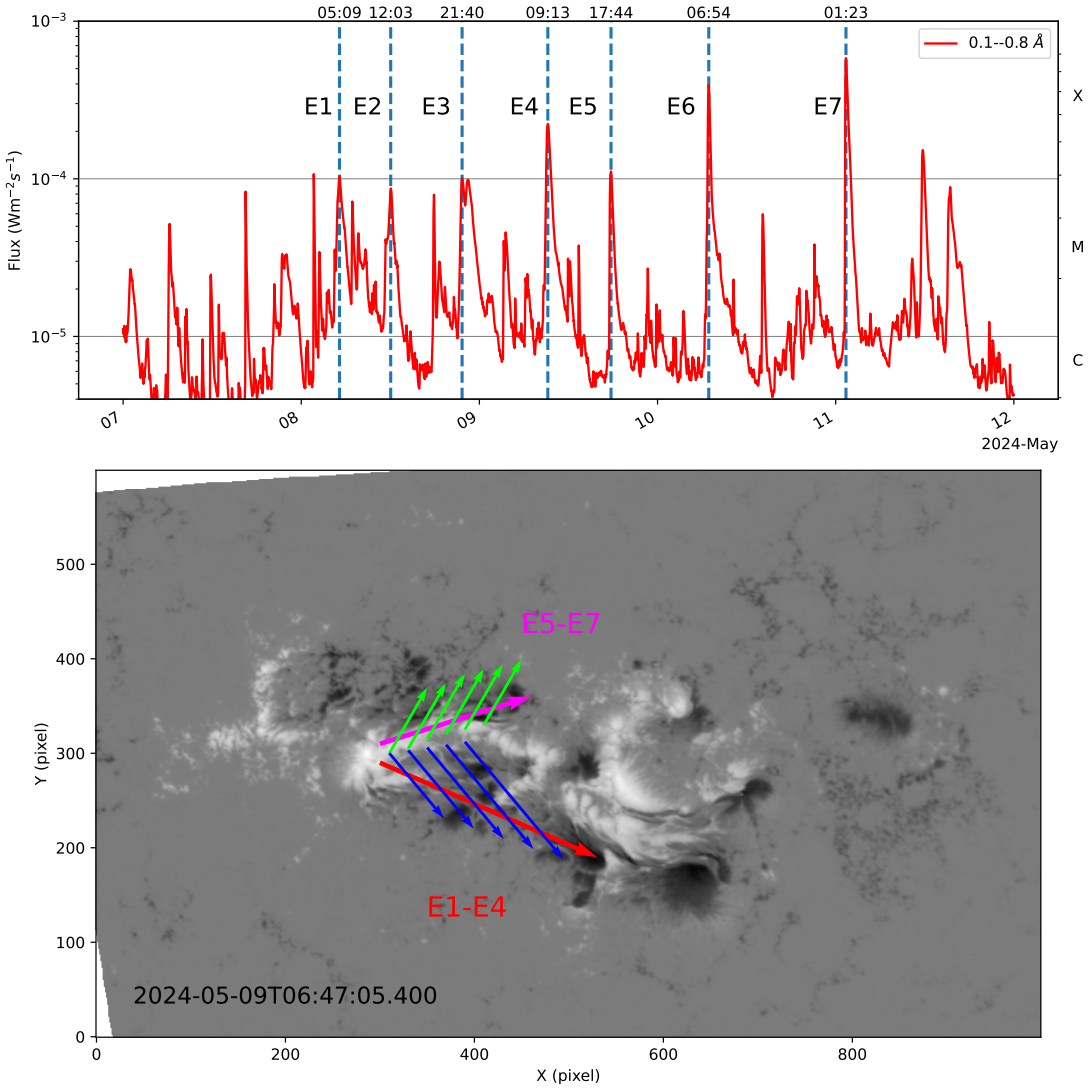

Fig. 1. Overview of GOES 1–8 Å flux (top) and AR 13664/8 (bottom). The vertical dashed blue lines show the flare peak times. The arrows indicate the axial fields of potential MFR structures along different PILs (red and purple), with reverse azimuthal fields (blue and green).

while comoving with the guiding center of the AR. To transform the cutout maps from the native helioprojective coordinate system into a local Cartesian coordinate system, we remapped the data using a cylindrical equal area (CEA) projection. Additionally, it is important to note that the observed LOS field is not truly radial, but rather projected onto the LOS. To obtain the radial magnetic field values B_r, we divided the original data $B_{\rm los}$ by μ, where μ represents the cosine of the angle between the LOS and the local normal at the solar surface.

The left column of Fig. 3 displays magnetograms, and ellipses of different colors outline the eruption source regions. These regions correspond to the nonconjugated collisional PILs of two sets of emerging dipolar magnetic fields. The ellipse is designed to maximally encompass the resultant high-gradient PIL, enabling a full tracking of variations in the magnetic field gradient that are caused by collisional shearing. The right column shows the B_r gradient map with a gradient exceeding the threshold of 500 G Mm^{-1}. Additionally, regions with a gradient exceeding 1000 G Mm^{-1} are marked with yellow contours. These are strong gradient areas. The comparison of the maps in the left and right columns shows that almost all eruption source regions exhibit high gradients along the collisional PILs. We calculated the cumulative sum of the strong gradients within the elliptical regions. Figure 4 demonstrates that each eruption (the vertical lines indicate the peak times of the flares) was accompanied by an increase in the cumulative gradient, which then gradually decreased after the eruption. This illustrates the strong correlation between the magnetic gradients and solar eruptions.

The AR exhibited a historically high magnetic flux emergence rate, with a maximum rate of approximately 1.6×10^{21} Mx h^{-1} over 6-hour intervals. It is worth noting that the magnetic field strength of this AR remained below 2000 G, which is significantly lower than for ARs with stronger magnetic field strength (e.g., AR 11944, >3000 G; Wang et al. 2015). It might be attributed to the exceptionally active flux emergence, which impedes the process of magnetic field concentration into high-strength polarities locally.

AR 13664 was preexisting, and its positive and negative magnetic polarites moved in opposite directions in the southeast-northwest direction. Subsequently, AR 13668 emerges to the east of AR 13664, undergoing a complex merging process with AR 13664, resulting in the formation of a more complex and

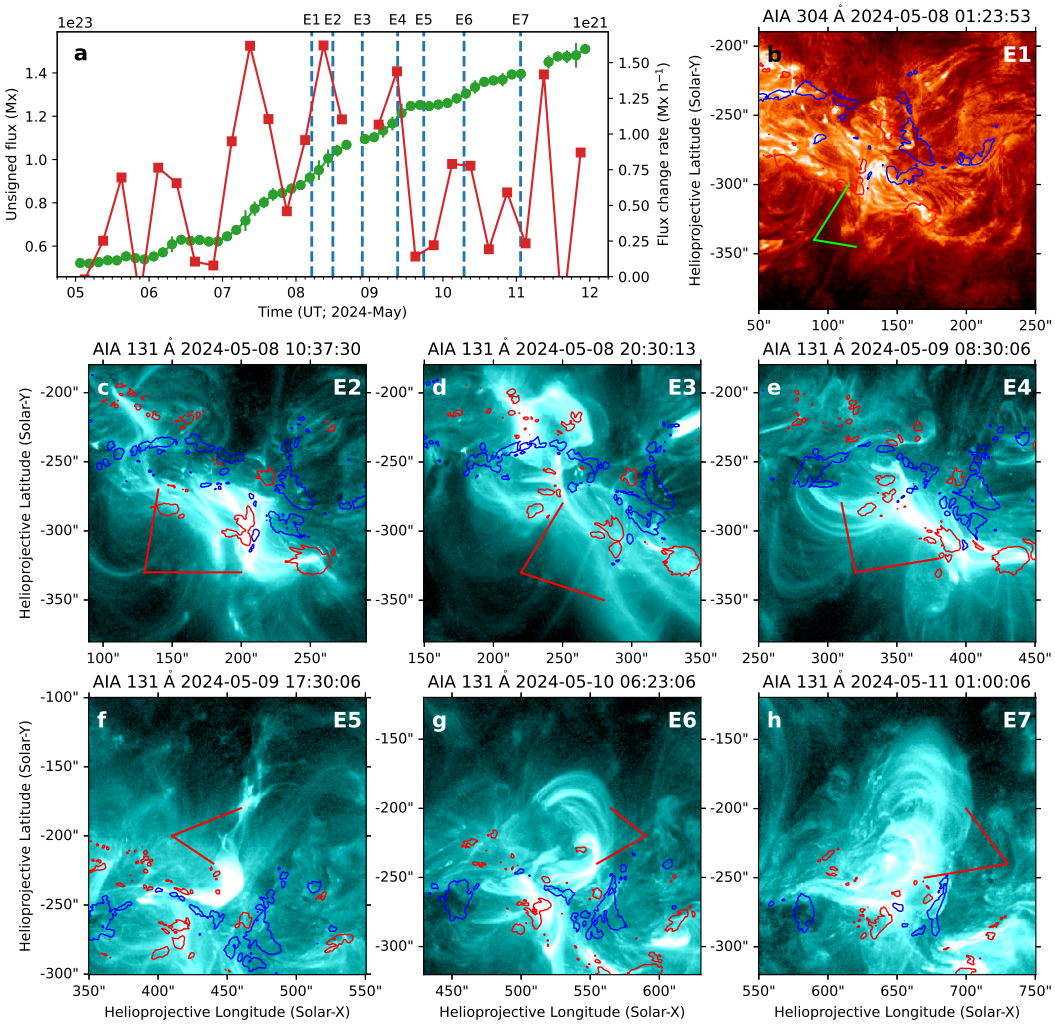

Fig. 2. Magnetic flux emergence and CME source regions. (a) Mean unsigned magnetic flux (green, 3-hour windows) and 6-hour average flux emergence rate of AR 13664/8 (red). The error bars are at 3σ within each window. (b)-(h) CME (E1-E7) source regions in AIA 304 Å and 131 Å. The green and red bars point to the locations of filament/hot channel. Positive (blue) and negative (red) fluxes (±1000 G) are overplotted.

large AR. We distinguished between dipole and nondipole field collisions through visual tracking of the magnetic poles. When positive and negative poles appeared simultaneously and moved synchronously in opposite directions, we identified them as a dipole pair. Since our goal is merely to identify dipole pairs rather than perform magnetic field calculations (e.g., magnetic flux cancellation), visual tracking suffices for this purpose. The early interaction is shown in Fig. 2b at locations (120″, −300″). E1 occurred at the nonconjugated magnetic PILs between P2-N3/N0 (see Fig. 3a) oriented in the north-south direction. Subsequently, E2 occurred at locations (170″, −260″; Fig. 2c). The B_r components of the two sets of nonconjugated magnetic polarities (P6-N5; Fig. 3b) are not very strong. Sun et al. (2024) revealed that the penumbra area of this region gradually expanded, implying that the magnetic field became more horizontal, with an increasing inclination angle. This distribution of magnetic fields in the photosphere is favorable for the formation of MFRs.

As mentioned before, the generation of large eruptions requires both the buildup of nonpotentiality and triggering factors. The collision of the nonconjugated magnetic fields (P3-N5) may serve as a trigger factor because flare E2 occurred directly above their convergence region while P3 and N5 continuously converged. It is likely associated with tether-cutting reconnection of reverse coronal magnetic fields above the PIL of P3-N5. We used a horizontal eclipse to calculate the total gradient of the E2 source region in Fig. 3. The left side of the ellipse exhibits evident shearing motion of P6 and N5 (Fig. 3b), which provides the necessary conditions for the buildup of MFRs (Chintzoglou et al. 2019; Wang et al. 2022). The occurrences of E3 and E4 can be seen as a sustained progression of the collisional shearing process that gave rise to E2. Once again, this pair of nonconjugated magnetic polarities (P3-N5/N6) interacted at positions (250″, −270″) and (350″, −270″), resulting in E3 and E4 (see Figs. 2d and 2e). We consider E2-E4 as a series of homologous eruptions. Notably, Fig. 2a reveals an exceptionally high average magnetic flux emergence rate of $\sim 10^{21}$ Mx h^{-1} during May 7-9. The peak emergence rate occurred on May 8 just before E2, and it was then followed by the other two consecutive homologous eruptions.

The location of E5 (410″, −240″) shifted to a more northern PIL (see Fig. 2f). The lower panel of Fig. 1 indicates that the azimuthal field around this set of PILs has a reverse direction with the lower set. Figs. 3a-d show that a pair of conjugated magnetic polarities (P4-N4) underwent a shearing motion, with the negative polarity N4 moving westward relative to the positive polarity. As the magnetic field gradient continued to

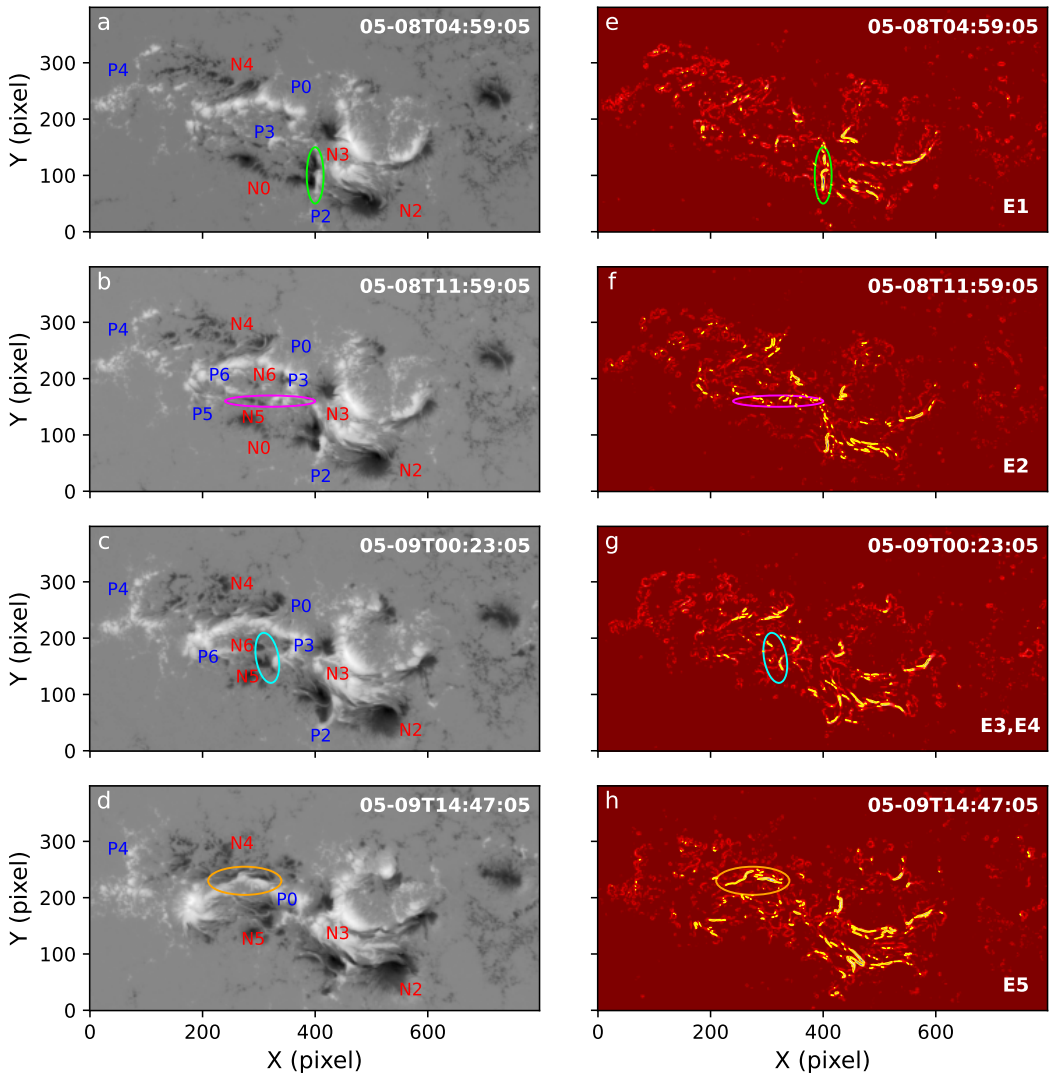

Fig. 3. B_r magnetograms (a-d) and their corresponding gradient maps (e-h) at sequential times. The color eclipses indicates the CME source regions. We show the dipolar magnetic fields. The yellow contours in (e-h) represent a strong gradient ($\geq$1000 G Mm^{-1}). The left and right columns correspond to two separate animations. A five-day animation of the magnetograms and gradient maps is available as an online movie, starting on 2024 May 4, 23:59 UT, and ending on 2024 May 9, 23:47 UT.

rise (Fig. 4d), E5 was triggered when a negative polarity rapidly intruded into the positive polarity P0. E6 and E7 shared the same PIL as E5. This PIL subsequently produced two even stronger X-class flares, X3.9 and X5.8 (as shown in Figs. 2g and 2h). Figure 2a indicates that these two eruptions coincided with periods of continued high magnetic flux emergence rates. However, as these two eruptions occurred in ARs beyond a longitude 30°W, where magnetic field data become unreliable, we did not calculate their gradients.

3. Conclusion and discussion

We examined the solar sources of the 2024 May geomagnetic superstorm, which was the largest storm in two decades. Our key findings reveal how photospheric magnetic configurations in eruption sources influence solar superstorm formation and geomagnetic responses, and link exceptionally strong flux emergence to sequential homologous eruptions. Our results are summarized below.

(1) Seven eruptions (E1-E7) occurred mainly along two primary PILs, as shown in Fig. 1. Based on a comparison of the AIA 131 Å high-temperature channel observations (Fig. 2), these source regions likely contained MFRs or sheared arcades as the initial magnetic field configuration for CMEs. Based on the photospheric magnetic field distribution, we roughly divided the source regions into two groups of homologous CMEs. The axial field of the first group (E1-E4) was generally aligned with the red arrow and the poloidal field was aligned along the blue arrows, both dominated by southward components. The second group (E5-E7) showed predominantly northward components in the axial and poloidal fields. Liu et al. (2024) identified two contrasting cases of complex ejecta in terms of their geoeffectiveness from in situ data. The first complex ejecta exhibited strong southward magnetic field components that contribute to the rapid decrease in the Dst index on May 10. The second showed weak southward fields that resulted in a slow Dst index recovery after May 13. The different magnetic field distributions around the eruption sources may explain their distinct geoeffectiveness, even though they both resulted from CME-CME interactions.

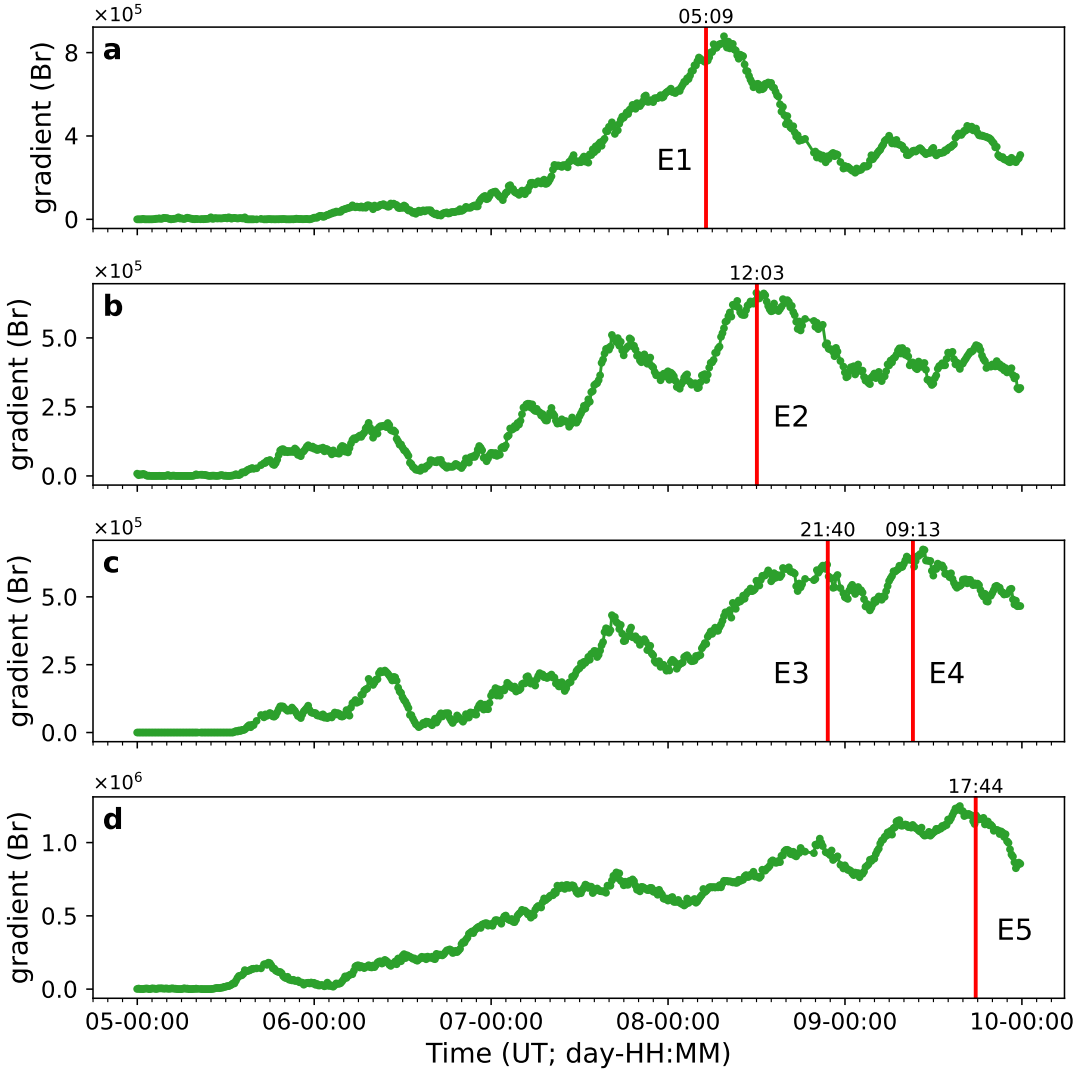

Fig. 4. Cumulative sum of strong gradients within the elliptical regions shown in Fig. 3. The vertical red lines correspond to E1-E5.

Li et al. (2024) presented the locations of flare ribbons that were observed in the SDO 1600 Å wavelength and white-light flares detected by ASO-S, which are consistent with our analysis of the magnetic field configuration in the eruption source region.

(2) Active region 13664/8 experienced historically strong magnetic flux emergence that peaked on May 8 at an exceptional rate of $\sim 1.6 \times 10^{21}$ Mx h^{-1}. From May 7-9, the average emergence rate sustained an extraordinarily high magnitude of $\sim 10^{21}$ Mx h^{-1}. Liu et al. (2024) noted that the CME associated with E5 exhibited a marked reduction in velocity relative to its predecessor. This velocity difference is thought to be directly linked to the formation of the two distinctly different complex ejecta mentioned above. According to the CME-CME interaction theory, the trailing CME needs to be faster than the leading CME to catch up and interact. Figure 2a shows that E5 (an X1.1 flare with 940 km/s; see Table 1 of Liu et al. 2024) occurred after the three-day period of the strongest average emergence rate, and both the associated flare and the CME speed were lower than E4 (an X2.2 flare with 1480 km/s). The significant drop in the emergence rate before E5 may explain its slower CME speed. The subsequent increase in the emergence rate for the following two eruptions demonstrates a correlation between the eruption intensity and the flux emergence rate.

(3) The detailed analysis of the photospheric magnetic field evolution near the erupting PILs revealed that these PILs can be classified as collisional PILs, as proposed by Chintzoglou et al. (2019). Our results indicate strong magnetic field gradients along these collisional PILs, which suggests a connection between gradient enhancement and eruption occurrence. The magnetic field gradients surrounding the PILs for all eruptions peaked at the onset of each event and were followed by a subsequent decrease in intensity. The gradient enhancement at the PILs is related to the converging motion of opposite-polarity fields on both sides of the PIL, driven by the collisional shearing process, which is induced by the superstrong magnetic flux emergence. This clarifies the underlying cause of the correlation between the eruption intensity and the emergence rate mentioned in (2). The collisional shearing efficiently converts the magnetic flux emergence into rapid accumulation of nonpotentiality that is necessary for eruptions. The continuous increase in the magnetic field gradients reflects the cumulative effect of the emerging flux at the PILs. According to Romano et al. (2024), photospheric velocity measurements revealed that the formation of this super AR underwent a sequence of phases, including the emergence phase, compaction phase, and shearing phase. This also effectively describes the complete collisional

shearing process. The compaction phase resulted in an extended collisional PIL that enhanced the magnetic field gradients in its vicinity.

The choice of magnetic field gradients as a key factor in assessing the eruptions is motivated by the direct consequences of the collisional shearing mechanism, which leads to the compression and increased densities of the magnetic fields on both sides of the nonconjugated magnetic polarities. Although the magnetic shear angle typically increases concomitantly, its variations do not always correspond directly to changes in the continuously emerging magnetic flux. When opposite magnetic poles are in close proximity, the shear angle tends to stabilize. Consequently, the impact of rapid magnetic flux emergence on eruptions is more effectively quantified by analyzing the changes in the magnetic field gradients around the PILs. The continuous increase in the gradient prior to the eruption is probably closely linked to the buildup of MFRs at the collisional PILs. When this gradient reaches a certain threshold, the further convergence of the two groups of magnetic fields likely induces local reconnection, which initiates the eruption. However, collisional shearing does not always simultaneously contribute to both nonpotential field buildup and eruption triggering. In most cases, it mainly affects the accumulation of the nonpotentiality. Triggering factors are more complex and include the previously mentioned kink and torus instabilities.

Factor such as MEANGBH, which was identified by Bobra & Ilonidis (2016) as a significant influence on the CME prediction, as well as earlier studies by Schrijver (2007) of the R factor and Dhakal & Zhang (2023) of SgPILs, all focus on changes in the magnetic field gradients along the PIL that are caused by active flux emergence. These factors, along with their derived quantities, are often used to evaluate the triggering mechanisms in ARs (e.g., Petrie 2012; Sun et al. 2015; Vemareddy 2017; Wang et al. 2018, 2022; Ran et al. 2022). In practice, there is often a focus on the overall gradient parameters of the AR or on all the PILs in general, and it is not specifically identified which high-gradient PILs are associated with eruptions. As shown in Figs. 3e-h, in addition to the eruption source region, high-gradient PILs are observed at various locations. When we can accurately measure the gradient changes that are directly associated with the source region, it will demonstrate a stronger correlation with solar eruptions. Additionally, to achieve a higher correlation, it is crucial to analyze large-scale eruptions that display substantial space weather effects and exhibit homologous properties in their eruption source regions. In this way, the stronger correlation can be better reflected. However, this may not facilitate prediction because we are not entirely certain which locations will experience eruptions. A better approach would be to focus on regions in which noticeable collisional shearing processes occur. If such a region has already experienced significant eruptions, there is a high likelihood of subsequent eruptions. We will consider conducting research in this area in the future.

Data availability

Movie associated to Fig. 3 is available at https://www.aanda.org

Acknowledgements. This research was supported by the Strategic Priority Research Program of the Chinese Academy of Sciences No. XDB0560000, NSFC under grant 12073032, the National Key R&D Program of China No. 2022YFF0503800 and No. 2021YFA0718600, and the Specialized Research Fund for State Key Laboratories of China. Y.D.L., X.W.Z., and H.D.H. also acknowledge support from NSFC under grants 42274201, 42204176, and 42150105, respectively. We acknowledge the use of data from SDO.

References

Bobra, M. G., & Ilonidis, S. 2016, ApJ, 821, 127
Bobra, M. G., Sun, X., Hoeksema, J. T., et al. 2014, Sol. Phys., 289, 3549
Chintzoglou, G., Zhang, J., Cheung, M. C. M., & Kazachenko, M. 2019, ApJ, 871, 67
Dhakal, S. K., & Zhang, J. 2023, ApJ, 960, 36
Fan, Y., & Gibson, S. E. 2004, ApJ, 609, 1123
Hoeksema, J. T., Liu, Y., Hayashi, K., et al. 2014, Sol. Phys., 289, 3483
Kliem, B., & Török, T. 2006, Phys. Rev. Lett., 96, 255002
Kliem, B., Titov, V., & Török, T. 2004, A&A, 413, L23
Lemen, J. R., Title, A. M., Akin, D. J., et al. 2012, Sol. Phys., 275, 17
Li, Y., Liu, X., Jing, Z., et al. 2024, ApJ, 972, L1
Liu, Y. D., Luhmann, J. G., Kajdič, P., et al. 2014, Nat. Commun., 5, 3481
Liu, Y. D., Zhao, X., Hu, H., Vourlidas, A., & Zhu, B. 2019, ApJS, 241, 15
Liu, Y. D., Hu, H., Zhao, X., Chen, C., & Wang, R. 2024, ApJ, 974, L8
Moore, R. L., Sterling, A. C., Hudson, H. S., & Lemen, J. R. 2001, ApJ, 552, 833
Okamoto, T. J., Tsuneta, S., Lites, B. W., et al. 2008, ApJ, 673, L215
Pesnell, W. D., Thompson, B. J., & Chamberlin, P. C. 2012, Sol. Phys., 275, 3
Petrie, G. J. D. 2012, ApJ, 759, 50
Ran, H., Liu, Y. D., Guo, Y., & Wang, R. 2022, ApJ, 937, 43
Romano, P., Elmhamdi, A., Marassi, A., & Contarino, L. 2024, ApJ, 973, L31
Scherrer, P. H., Schou, J., Bush, R. I., et al. 2012, Sol. Phys., 275, 207
Schou, J., Scherrer, P. H., Bush, R. I., et al. 2012, Sol. Phys., 275, 229
Schrijver, C. J. 2007, ApJ, 655, L117
Sun, X., Bobra, M. G., Hoeksema, J. T., et al. 2015, ApJ, 804, L28
Török, T., Kliem, B., & Titov, V. 2004, A&A, 413, L27
van Ballegooijen, A. A., & Martens, P. C. H. 1989, ApJ, 343, 971
Vemareddy, P. 2017, ApJ, 851, 3
Wang, R., Liu, Y. D., Dai, X., et al. 2015, ApJ, 814, 80
Wang, R., Liu, Y. D., Hoeksema, J. T., Zimovets, I. V., & Liu, Y. 2018, ApJ, 869, 90
Wang, R., Liu, Y. D., Yang, S., & Hu, H. 2022, ApJ, 925, 202
Woodgate, B. E., Martres, M. J., Smith, J. B., J., , et al. 1984, Adv. Space Res., 4, 11
Zhang, J., & Wang, J. 2002, ApJ, 566, L117